Correspondence to:
K. M. Christensen,
katyc4@uw.edu

Global Estimates of Mesoscale Vertical Velocity Near 1,000 m From Argo Observations

Katy M. Christensen[1] , **Alison R. Gray[1]** , and **Stephen C. Riser[1]**

[1]School of Oceanography, University of Washington, Seattle, WA, USA

Abstract Global estimates of mesoscale vertical velocity remain poorly constrained due to a historical lack of adequate observations on the spatial and temporal scales needed to measure these small magnitude velocities. However, with the wide-spread and frequent observations collected by the Argo array of autonomous profiling floats, we can now better quantify mesoscale vertical velocities throughout the global ocean. We use the underutilized trajectory data files from the Argo array to estimate the time evolution of isotherm displacement around a float as it drifts at 1,000 m, allowing us to quantify vertical velocity averaged over approximately 4.5 days for that depth level. The resulting estimates have a non-normal, high-peak, and heavy-tail distribution. The vertical velocity distribution has a mean value of $(1.9 \pm 0.02) \times 10^{-6}$ m s^{-1} and a median value of $(1.3 \pm 0.2) \times 10^{-7}$ m s^{-1}, but the high-magnitude events can be up to the order of 10^{-4} m s^{-1}. We find that vertical velocity is highly spatially variable and is largely associated with a combination of topographic features and horizontal flow. These are some of the first observational estimates of mesoscale vertical velocity to be taken across such large swaths of the ocean without assumptions of uniformity or reliance on horizontal divergence.

Plain Language Summary Vertical velocity in the ocean is a fundamental part of how water circulates throughout the globe. This impacts the temperature, salt, nutrients, and currents that make up the ocean. However, vertical velocities are very small and are, therefore, difficult to measure. In particular, the vertical velocities of ocean events that occur on roughly a weekly to monthly time scale (mesoscale) are poorly understood. We have developed a method for estimating these mesoscale vertical velocities across the globe using an array of autonomous robots called Argo floats. Our results show that vertical velocities vary greatly depending on location, with the largest values occurring where there is a combination of relatively shallow ocean depths and larger horizontal velocities. These estimates are some of the first of their kind to be made from observations across such large swaths of the ocean.

1. Introduction

An essential component of many physical, chemical, and biological processes, vertical motion in the ocean occurs at all spatial and temporal scales, with a high degree of variability in both. As the pathway from the ocean interior to the surface, vertical flow directly impacts thermocline structure, nutrient transport, and global circulation (Liang et al., 2017; Martin & Richards, 2001; Munk, 1966; Pilo et al., 2018; Stommel & Arons, 1959; Sverdrup, 1947). At the largest scales, the highly idealized model created by Stommel and Arons (1959) first estimated vertical velocities ranging between 0.5 and 3.0×10^{-7} m s^{-1}, averaged over large areas of the deep ocean, to compensate for dense water formation at high latitudes. As the spatio-temporal scale of the motions decrease, the magnitude of the associated vertical velocities tends to increase, as well as the variability across regions. The time-averaged vertical velocity at mid-depths associated with mesoscale motions has been estimated to be on the order of 10^{-6} m s^{-1} in a model (Liang et al., 2017), while values on the order of 10^{-4} m s^{-1} have been estimated within coherent vortices (Martin & Richards, 2001; Pilo et al., 2018). Small-scale vertical velocities observed at mid-depths within internal waves and lee waves have been estimated to be on the order of 10^{-2} m s^{-1} (Merckelbach et al., 2010) and 10^{-1} m s^{-1} (Cusack et al., 2017), respectively. While these smaller-scale estimates are often inferred from observations at the locations and depths where phenomena at these scales occur, estimates at meso and larger scales are commonly determined from numerical models that do not resolve the small-scale processes, horizontally or vertically. Directly observing vertical velocities in the ocean at these scales has been an enduring challenge, due to the small magnitudes and high spatio-temporal variability (Liang et al., 2017; Martin & Richards, 2001; Stommel & Arons, 1959).

Despite the inherent difficulties, estimates of vertical velocities have previously been computed using observations across different scales, depths, and geographic locations, from many different sources including hydrographic profiles (Martin & Richards, 2001; Munk, 1966; Stommel & Arons, 1959), moorings (Sévellec et al., 2015), floats (Cusack et al., 2017; Freeland, 2013), and gliders (Frajka-Williams et al., 2011; Merckelbach et al., 2010). However, these estimates are often only able to capture either large- or small-scale vertical velocities due to limited sampling area or necessary assumptions of uniformity in depth and across smaller scales (Freeland, 2013; Liang et al., 2017; Stommel & Arons, 1959). The vertical velocities of mesoscale phenomena, which have horizontal scales of ~100 km, are not particularly well observed, even though such motions are in one of the most dynamic energy bands in the ocean (Ferrari & Wunsch, 2009). Because mid-depth mesoscale velocities—both horizontal and vertical—are historically poorly characterized from observations, constraints on these flows in numerical models are completely lacking (Zilberman et al., 2023). Oceanic models such as those used for coupled climate projections may therefore be misrepresenting these vertical motions and the associated fluxes of tracers. To advance our understanding of this critical component of the oceanic velocity field, a novel approach is needed to greatly expand our ability to estimate vertical velocities in the global ocean from observations.

The observations collected by the Argo array of profiling floats constitute the largest global, open-ocean, subsurface oceanic data set. Since the late 1990s, the Argo program has vastly increased the coverage and quality of oceanographic observational data (Roemmich et al., 2019). The classic Argo float cycle consists of a descent to 1,000 dbar, a drift with the flow at that level in a quasi-isobaric fashion for approximately 10 days, another descent to 2,000 dbar, an ascent to the surface while taking profile measurements of conductivity, temperature, and depth (CTD), and finally the transmission of data collected during the cycle to data acquisition centers using Iridium communications. The profile data from 0 to 2,000 dbar are well-organized by the Argo program, comprehensively quality controlled, and have been extensively used in oceanographic research (Riser et al., 2016; Roemmich et al., 2019; Wong et al., 2020). Argo float profiles have previously been used to estimate vertical velocities in the open northeast Pacific (Freeland, 2013); however, that large-scale bulk estimate relied on computing the divergence within a well-defined control volume. Expanding this method to retrieve global vertical velocities at a finer scale, across a wide range of dynamic regimes, would require consideration of further processes and flows with the resulting uncertainties quickly dominating the estimates.

In addition to the profiles of temperature and salinity collected at the end of each cycle, a large number of Argo floats also record temperature and pressure measurements during the drift at 1,000 dbar. The vast majority of floats do not measure salinity during the park phase. The temperature and pressure park phase data have been less frequently utilized than the profile measurements, and the associated quality control has been less consistent across platforms. Drift data at hourly resolution have previously been used to compute high-frequency isotherm displacement relative to the quasi-isobaric float, in order to examine internal wave characteristics near 1,000 dbar (Hennon et al., 2014). The observations recorded during the drift phase of Argo floats remain, however, relatively untapped as a source of information about the subsurface ocean. The work presented here uses these data to estimate mesoscale (~5-day mean) vertical velocities at mid-ocean depths. The resulting near-global picture of the vertical flow at 1,000 m, quantified directly from observations for the first time at such scales, not only reveals important patterns of spatial variability but also provides a critical benchmark for the subsurface flow in numerical models.

Section 2 introduces the analysis framework underlying the method we have developed to estimate vertical velocity using data recorded during an Argo float's drift phase. In Section 3 we apply the theory to the global Argo database and detail the extensive quality control steps that we have taken to ensure consistency in our estimates. The resulting vertical velocity estimates are presented in Section 4, and several key geographic areas are highlighted. Additionally, we investigate how our estimates of vertical velocity relate to geographic location, bathymetry, horizontal flow, and Sea Level Anomaly (SLA). Finally, Section 5 compares the Argo-based estimates to model-based vertical velocities and discusses the implications of our results.

2. Theoretical Framework

To develop a method for estimating vertical velocity from high-frequency data recorded during the drift of Argo floats, we start with the evolution of temperature T following a water parcel

$$\frac{DT}{Dt} = k_z \frac{\partial^2 T}{\partial z^2} + k_h \left(\frac{\partial^2 T}{\partial x^2} + \frac{\partial^2 T}{\partial y^2} \right) + Q \tag{1}$$

where $k_z \frac{\partial^2 T}{\partial z^2}$ represents the rate of change in temperature due to vertical mixing including the vertical diffusivity k_z, $k_h \left(\frac{\partial^2 T}{\partial x^2} + \frac{\partial^2 T}{\partial y^2} \right)$ represents the rate of change in temperature due to horizontal mixing including the horizontal diffusivity k_h, and Q corresponds to the rate of change in temperature from external sources and sinks of heat. Consider now the temperature evolution of a water parcel at mid-depths in the open ocean, over approximately 5 days. For the associated space and time scales, we can assume that the influence of horizontal mixing on temperature (following a water parcel) is negligible. In addition, if the vertical temperature gradient $\frac{dT}{dz}$ is constant, the contribution of vertical mixing will vanish. Thus, given these conditions are upheld, we can neglect the temperature change due to mixing altogether.

In the open ocean there are negligible sources and sinks of heat at the float parking depth of 1,000 dbar, so we can also approximate Q as zero. Thus, we are left with $\frac{DT}{Dt} \approx 0$, which can be expanded to show the contribution due to advection by both horizontal and vertical velocities (u_H and w, respectively),

$$\frac{\partial T}{\partial t} + u_H \cdot \nabla_H T + w \frac{\partial T}{\partial z} \approx 0. \tag{2}$$

Applying this framework now to an ideal, completely isobaric float that perfectly follows the horizontal projection of the flow causes the horizontal velocity relative to the float, u_H, to vanish. In other words, the temporal evolution of temperature observed by the float as it is drifting with the horizontal flow will solely reflect the vertical advection of the background temperature gradient. Further decomposing the temperature into a time-averaged mean $\bar{T}$ and a time-varying anomaly T' and assuming that the temperature gradient at depth is constant at these spatial and temporal scales allows Equation 2 to be solved for w as

$$w = -\frac{\partial(T' + \bar{T})}{\partial t} \Big/ \frac{\partial T}{\partial z} \approx -\frac{d}{dt} \left(T' \Big/ \frac{\partial T}{\partial z} \right). \tag{3}$$

Thus, vertical velocity at the park depth can be computed from the observed rate of change of isotherm displacement relative to the float.

Moving from a theoretical particle to a real world float, we must consider that the float is not perfectly isobaric. In fact, the floats move on equilibrium surfaces defined by their mass, which deviate from pressure surfaces depending on surrounding conditions and float compressibility (Swift & Riser, 1994). Following Hennon et al. (2014), we account for the vertical motion of an Argo float away from the 1,000-dbar isobar by subtracting the float displacement, given by the pressure anomaly during the drift. Doing this ensures that the isotherm displacement we estimate is a product of fluid motion alone. We then incorporate the pressure correction term into Equation 3. The pressure measured by a float must also be converted into units of depth to give velocity in m s^{-1}, which can be done by assuming a hydrostatic balance $\left(z = \frac{P}{\rho g} \right)$. Following this we are left with the following equation for w:

$$w = -\frac{1}{\rho g} \frac{d}{dt} \left(\frac{T'}{(dT/dP)_{1000}} - P' \right) \tag{4}$$

where T' is the park phase temperature anomaly defined by $T' = T - \bar{T}$ with $\bar{T}$ being the time average temperature, P' is the park phase float displacement defined by $P' = P - \bar{P}$ with $\bar{P}$ being the time average pressure, $(dT/dP)_{1000}$ is the constant temperature gradient at 1,000 dbar, ρ is the local density at 1,000 dbar, and g is the gravitational constant. This final equation allows us to estimate vertical velocity solely using data from Argo floats, with T' and P' calculated from the float trajectory data and with $(dT/dP)_{1000}$ and ρ calculated from the float profile data.

3. Estimation of Argo-Float Based Vertical Velocity

3.1. Global Argo Data

Data used in this work include the drift trajectory, profile, technical (e.g., float systems reports during cycles), and metadata (e.g., float cycle configuration information) for the global array of Argo floats. Though there are over 16,000 floats with trajectory information available in the Global Data Acquisition Center, many of the cycles from these floats cannot be used in estimating vertical velocity. Data that are useable for these estimates start in August 2005 and continue through April 2022. Data prior to 2005 are not useable because early float versions

did not report an adequate number of samples during the drift cycle. Additionally, some later data are not useable because floats deployed by different programs or from different manufacturers report the drift data inconsistently with one another causing the necessary trajectory information to be less-uniformly available compared to that of the profile data. The biggest discrepancy is in the sampling regime during the park cycle, which results in floats reporting data ranging from sparse drift averages up to comprehensive hourly measurements of temperature and pressure. Note that the technical data and metadata for floats are similar to the trajectory data in that they are inconsistently implemented between float programs. This can lead to missing file components causing the data from a float to be unusable in estimating vertical velocity. In particular, we are unable to use cycles that report temperature and pressure less frequently than every 6 hr during the park phase as well as cycles that have inadequate geographic coordinates, cycle numbering, and time information. To ensure that our results are as robust as possible, we have designated several quality control parameters (Section 3.3) in addition to the Argo program quality control system (Wong et al., 2020). In consequence, our vertical velocity estimates are gleaned from 998 floats, encompassing 107,144 estimates.

3.2. Methods

From Equation 4, both the temperature gradient, $(dT/dP)_{1000}$, and the density, ρ, at 1,000 dbar are found using float profile measurements. To get representative values for the entire park phase, the profiles directly before and after each individual park phase are averaged. The density at 1,000 dbar is computed using the Gibbs-SeaWater Oceanographic Toolbox routines created by McDougall and Barker (2011) and is a function of absolute salinity and conservative temperature at a constant pressure of 1,000 dbar. The temperature gradient is determined by finding the least squares best-fit line to the averaged temperature profile within 100 dbar from the parking depth (Hennon et al., 2014) (Figure 1b).

Starting with the raw temperature and pressure data reported during the entire float park, each drift cycle is split into a half-cycle of at least 4 days in length. The temperature and pressure anomalies during the park, T' and P', are found by subtracting the half-cycle mean values from the data for each half-cycle (Figure 1c). These anomalies are then applied to Equation 4 to find the corrected isotherm displacement (Figure 1d). To examine phenomena on longer than inertial time scales, we use a fourth order lowpass Butterworth filter with a cutoff frequency of 0.3 cycles per day on the corrected isotherm displacement with odd reflected endpoints. This effectively removes high frequency variability caused by internal tides and other short-lived events (Hennon et al., 2014). After filtering, we fit the data using a piecewise cubic Hermite interpolating polynomial (pchip) (Fritsch & Carlson, 1980) and take the derivative with respect to time to get the slopes of the data during the drift half-cycle. Taking the average of this derivative and converting to depth units using float profile density in the equation for hydrostatic balance (the same assumption made to reach Equation 4), gives us approximate values for the half-cycle-average vertical velocity (Figure 1e).

3.3. Quality Control

After a measurement cycle occurs, floats transmit their data to the data acquisition centers via the Argos-2 (<1% of useable floats) or the Iridium (>99% of useable floats) satellite systems. Then the data go through an automated quality control process that checks for reasonable dates, locations, velocities, pressures, temperatures, and salinities (Argo User's Manual, 2022; Wong et al., 2020). Values are flagged with identifiers ranging from 1 to 4, where 1 corresponds to good data and 4 corresponds to bad data. This project uses quality control flags equal to 1, 2, or data that have been adjusted to reach the same level of qualification (Wong et al., 2020). Within 24 hr after a float surfaces, the data have gone through the process described above and are publicly available as *Realtime-mode* data. In the following 5 months, more rigorous quality control should be done updating the cycle label to *Delayed-mode* (Wong et al., 2020). However, this step is often only applied to the profile data and not to the trajectory, technical, or metadata files. For estimating vertical velocity, we use the *Delayed-mode* data for the selection of floats where it is available (23.5% of useable cycles) and the *Realtime-mode* data in all other cases.

As stated in Section 2, the vertical temperature gradient must be linear to maintain the assumption that there are limited vertical mixing effects on temperature. To enforce this condition, only cycles where the least squares best-fit line accounts for at least 90% of the temperature variance are considered (Hennon et al., 2014). In some cases, the slope estimated from the profile data was near zero resulting in the magnitude of our vertical velocity
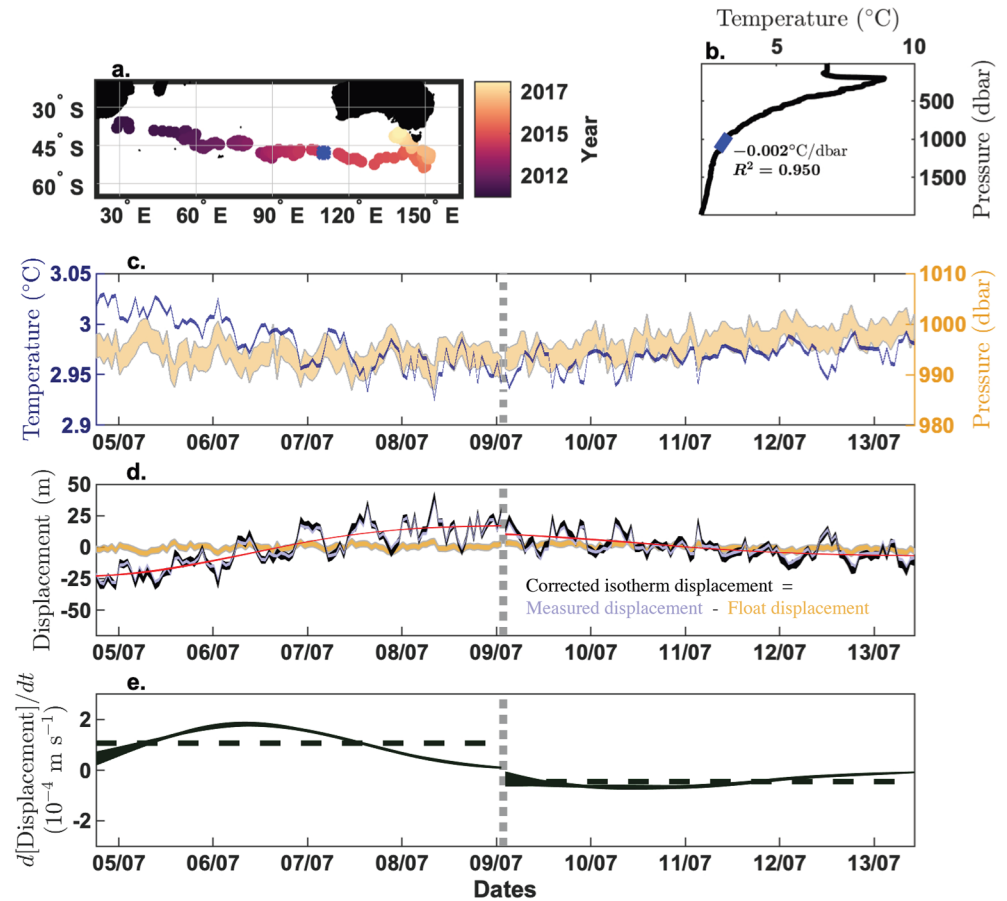
Figure 1. Example process for estimating vertical velocity using cycle number 134 from float 1901150 (WMO ID). No float buoyancy adjustments occurred during this cycle, so we are able to estimate two vertical velocities, one on each side of the gray dashed line in each panel. (a) Map of all float cycle locations colored by date taken, except cycle number 134 which is noted in blue. (b) Profile of temperature and pressure from cycle 134 with data surrounding 1,000 dbar used to calculate $(dT/dP)_{1000}$, with at least 90% linear fit, highlighted in blue. (c) Hourly sampled trajectory data where the temperature (blue) is shaded as the envelope of 100 iterations of added random error of $\pm 0.002°C$ and the pressure (orange) is shaded as the envelope of 100 iterations with added random error of ± 2.4 dbar, as used in the Monte Carlo simulation described in Section 3.3 (d) Corrected isotherm displacement (black), calculated by subtracting float displacement (orange) from total measured displacement (blue), $\left[\frac{T'}{(dT/dP)_{1000}} - P'\right]$. The corrected isotherm displacement is then filtered using a fourth Order Lowpass Butterworth filter and fit using a pchip function (red). Note that all of these values are converted to meters using an assumption of hydrostatic balance. (e) Derivative of the filtered corrected isotherm displacement (solid black) and average value of the derivative (dashed black), which results in vertical velocity estimates of $(7.6 \pm 0.1) \times 10^{-5}$ m s^{-1} and $(-3.0 \pm 0.1) \times 10^{-5}$ m s^{-1} on the left and right sides of the cycle, respectively. Note that the error of these estimates is taken from the standard deviation of the 100 estimates that resulted from the Monte Carlo iterations.

estimates being unreasonably large. To counteract these cases, any vertical velocity with a magnitude larger than 10 standard deviations away from the mean of all the estimates are neglected (<0.05% of estimates).

Due to differences in float manufacturing and measurement goals, not all floats are programmed in the same manner. In particular, floats do not all have the same parking pressure and do not report data at the same interval during the drift. To keep the vertical velocity estimates comparable to one another, only floats that are assigned a park pressure of 1,000 dbar in their metadata have been used. For differing drift data intervals, only floats that report both temperature and pressure measurements at a minimum of 6-hourly time increments during the park phase have been included. Previous studies that have analyzed isotherm displacement during the drift cycle could only use hourly-reporting floats because they were trying to capture the signal from internal gravity waves and tides (Hennon et al., 2014). The mesoscale vertical velocities we are estimating persist over somewhat larger time scales, so we can use floats with a longer time between samples. As confirmation that the 6-hourly floats

supply sufficient resolution, we conducted a test where we sub-sampled the hourly floats to every 6 hr, with randomly selected initial points, and re-estimated the vertical velocity using our method. When comparing the initial velocity estimates from the hourly samples with those from the sub-sampled regime, there is a 91% correspondence in the linear fit; the slope of this linear fit is 0.87. Though the 6-hr sub-sampling does slightly cause our method to underestimate the vertical velocity magnitude, particularly at large values, we feel that this error is sufficiently small with the average difference between the 6-hr sub-sampled values and the hourly true values being 2.2×10^{-7} m s^{-1}. Floats that measure once per day or transmit a cycle average value do not capture the necessary temperature variability to estimate isotherm motion around the float and are therefore discarded.

To maintain the programmed park pressure, floats will internally adjust their buoyancy under certain conditions. If a float is pushed outside of a pre-determined threshold (most often ± 10 dbar, located in the float metadata) from the programmed park pressure for 3 hr consecutively, the float increases or decreases its buoyancy to move back into the target zone. This adjustment causes additional variability in temperature measurements that is difficult to distinguish from temperature variability caused by isotherm displacement alone. Buoyancy adjustments can happen multiple times in a single drift cycle and the floats then report the number of times that they adjust in their technical data; however, they do not report when the adjustments actually occur. To manually determine when an adjustment happens, hourly data are required. Thus, for floats with a lower sampling frequency than hourly any cycles with reported adjustments are discarded. For floats that do measure on an hourly basis, we use the pressure data to compute the time of adjustment and keep only those cycles where the number of computed adjustments equals that reported in the technical data. Only half-cycles with no adjustments (omitting data in a 6 hr window after any prior adjustments) were used to compute vertical velocity. The floats do adjust preferentially in certain areas, which can likely be attributed to large magnitude vertical motions influencing the floats. Because we are neglecting cycle halves that include these adjustments, the estimates for vertical velocities shown in this paper can be considered conservative.

To estimate the error involved in calculating the vertical velocity, we have conducted a Monte Carlo simulation that incorporates random error based on instrument accuracy. Floats are equipped with CTD sensors that have published accuracy of $\pm 0.002°$C (0.0002°C drift per year) and ± 2.4 dbar (0.8 dbar drift per year) for temperature and pressure, respectively (Wong et al., 2020). Because the average values are removed during the calculations, the precision of each measurement is more likely to impact the observation quality, but these values are smaller than those of the accuracy. We feel confident that using the larger values allows for robust testing in the Monte Carlo simulation. For each calculation of vertical velocity, 100 iterations of random error within the accuracy ranges were incorporated into the temperature and pressure data. These data were then used to compute 100 estimates of vertical velocity for each half cycle. The final value is the average of all the different iterations and the error is assumed to be represented by the standard deviation (Figure 1c). To compute aggregate statistics (mean, median, variance, etc.) on subsets of the data, we use all 100 of the Monte Carlo iterations for each half cycle and report the average of the desired statistic along with the standard deviation as our error estimate.

4. Results

4.1. Global Estimates of Near 1,000-m Vertical Velocity

The locations of vertical velocity estimates from the global Argo array have a spatial distribution that varies widely across geographic regions (Figures 2a–2c). Though the Argo array is well-distributed globally (Wong et al., 2020), these estimates of vertical velocity do not have uniform coverage and are particularly sparse in the Atlantic and North Pacific Oceans (Figure 2c). This is due to a lack of adequate 1,000 dbar drift data in those areas in addition to a rigorous application of quality control measures (Section 3.3).

The estimated vertical velocities have a particularly heavy-tailed distribution with a high peak (Figure 3). These data have the smallest sum square error (defined as $\sum_i (y_i - f(x_i))^2$, where y_i is the given histogram value and $f(x_i)$ is the value predicted by the probability density function) when fit by the Cauchy function as Equation 5,

$$f(x) = \frac{1}{\pi(1 + x^2)} \tag{5}$$

which is the equivalent to a Student's t continuous fit with one degree of freedom (Forbes et al., 2010). In comparison, a normal distribution is equivalent to a Student's t continuous fit with infinite degrees of freedom, meaning
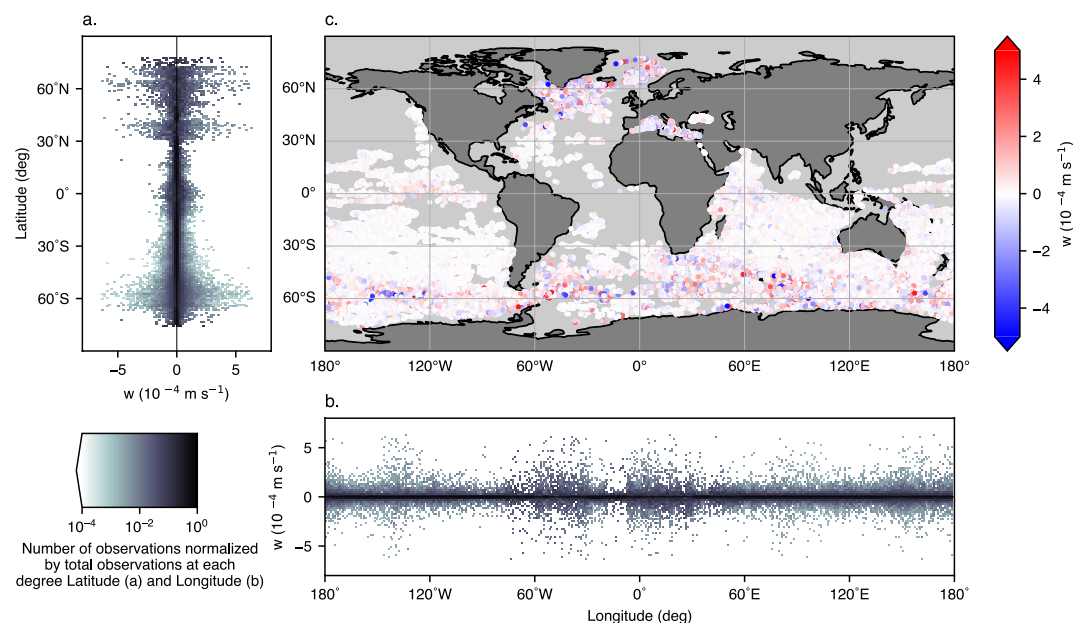
Figure 2. Argo-based, 5-day-averaged vertical velocities near 1,000 m. Probability density functions of velocities as a function of (a) latitude and (b) longitude, normalized at each degree latitude or longitude, respectively. (c) Global map of all individual velocity estimates.

that these data are decidedly non-Gaussian (Forbes et al., 2010). One characteristic of a Cauchy probability distribution is that the higher order statistical moments are undefined and do not converge with increased sampling (Forbes et al., 2010; Sugiyama, 2016). Therefore, the mean and standard deviation that we compute for our finite data set are highly dependent on the selection of sampling parameters and do not converge for large sample size. To characterize our data set, we compute and report the median, which is less influenced by heavy tails. We also examine the mean and standard deviation for our data with the caveat that these values are dependent on the particular characteristics of sampling. With this in mind, this type of statistical analysis can still help provide insight into the variability of our estimates.

The median vertical velocity from the entirety of our estimates, is $(1.3 \pm 0.2) \times 10^{-7}$ m s^{-1} and the average vertical velocity is $(1.9 \pm 0.02) \times 10^{-6}$ m s^{-1}. If these data were collected everywhere globally, over a sufficiently long time period, the true average would be equivalent to zero due to the conservation of mass in the ocean (Freeland, 2013; Stommel & Arons, 1959). However, there is no evidence to suggest that the vertical motion occurring at just the mesoscale should be balanced within itself, so we cannot assume that the average of our irregularly-sampled, mesoscale estimates should be equal to zero. The variance of our vertical velocity estimates is $(3.0 \pm 0.01) \times 10^{-9}$ [m s^{-1}]^2, which is impacted by both the high peak and heavy-tails of our distribution. There is a slight positive skew of 0.6 ± 0.03; however, due to the shape of the distribution discussed above, we cannot disentangle if this is a product of the uneven spatial and temporal distribution of our samples or a product of actual physical phenomena. To gain different insights into these estimates, we examine areas that are well sampled in context with SLA.
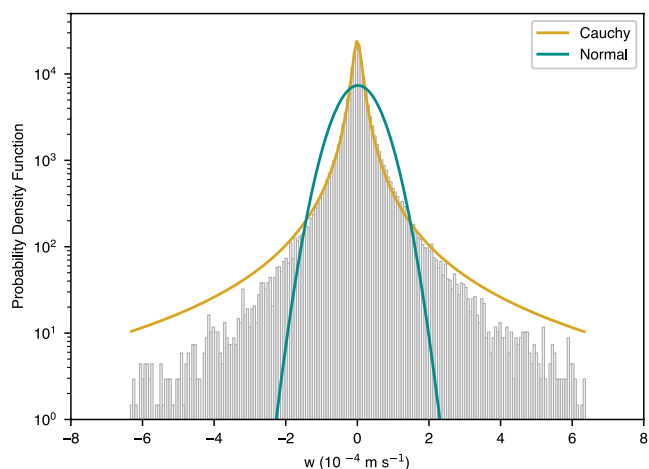

Figure 3. Probability density function (PDF) of global vertical velocities with Cauchy (gold) and Normal (teal) distributions plotted atop. Note that the *y*-axis is on a logarithmic scale.

4.2. Sea Level Anomaly

To examine how our mid-depth vertical velocity estimates correspond with other physical phenomena in the ocean, we use the Data Unification and Altimeter Combination System (DUACS) gridded (L4) altimeter product with a 1/4° × 1/4° resolution with daily data ranging from 1993 to June 2020 (CMEMS, 2021). From this gridded product, we use both the SLA and the
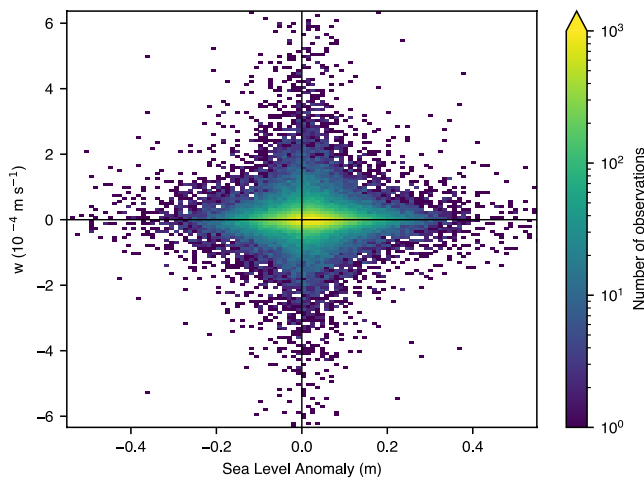
Figure 4. Global Sea Level Anomaly (SLA) versus vertical velocity estimates colored by the number of observations for each $0.01 \text{ m} \times 10^{-5} \text{ m s}^{-1}$ box.

horizontal (zonal [U] and meridional [V]) absolute geostrophic velocities at the surface.

The SLA in this data set is given as the sea surface height above mean sea surface using a 20-year mean from 1993 through 2012; however, to better compare this data with that given by the Argo array, we have changed the reference period to be a 15-year mean from 2005 through 2020 following the methods in Pujol et al. (2016). To directly link float estimates with satellite SLA, we located the nearest grid cell in the DUACS L4 product to each vertical velocity estimate location and averaged the SLA at that point for the actual dates of the float cycle. We repeat the process for the horizontal velocity magnitude, computed from surface U and V, by finding the nearest grid cells in the satellite product to our float estimates. However, we then average across all times (1993–2012) rather than just the float period. Taking the average over the entire time-series results in a mean state horizontal velocity, to which we can compare our vertical velocity.

Investigating the SLA from all locations where we have half cycles, we see that there is no distinct correlation between the SLA and the vertical velocity estimates (Figure 4). The highest values of vertical velocity would visually appear to be associated with smaller magnitude SLA, but there are considerably more data points present at smaller magnitudes than at higher magnitudes for both the vertical velocity and SLA (note Figure 4 has an exponential colorbar). Statistically this pattern is simply a product of the high peaks in both the vertical velocity and SLA distributions rather than showing a particular physical phenomena. Additionally, the SLA is measured at the surface via satellites, so comparing these measurements to our mid-depth estimates of vertical velocity is not direct. Certainly, not every eddy has a subsurface component that will have an effect at the Argo parking depth. There are ways to locate sub-surface phenomena solely using satellite data (Assassi et al., 2016); however, these methods have difficulty in complex areas with strong currents, of which a great deal of our study area is composed. Instead, separating our vertical velocity estimates and their associated SLA into subsets of areas with high coverage will allow us to examine the degree of variability between different locations.

4.3. Spatial Variability and Areas of Interest

Because of the varying data density across the globe, spatial analysis of the entire data set is not wholly informative. Looking closer at the variation in longitude (Figure 2b), we can see that the higher magnitude velocities do not occur uniformly, but instead have a unique distribution with certain areas being hot spots of higher magnitude vertical velocity. We have selected a few key areas for comparison. Namely, we chose two major topographic features in the Antarctic Circumpolar Current (ACC) in the Southern Ocean (Kerguelen Plateau [KP] and Pacific-Antarctic Ridge [PAR], Figures 5d and 5e) and selected juxtaposed examples in the gyres north of each (Indian Ocean Gyre [IOG] and Pacific Ocean Gyre [POG], Figures 5b and 5c). Each of these subsets of data has a comparable number of observations rather than equal study areas. The ACC generates considerable mesoscale and submesoscale variability that is expected to be associated with higher magnitude vertical velocities (Cusack et al., 2017; Rosso et al., 2014).

We find that the distributions of vertical velocity estimates over topographic features are similar to the global distribution in that they have high peaks and heavy tails that are best fit by the Cauchy function (Figures 5d and 5e). Our estimates in quiescent areas have much lighter tails and, though still not entirely normally distributed, are better fit by a normal distribution across most of the estimates with the only misfits being infrequent, high-magnitude events appearing in the tails (Figures 5b and 5c).

The median, mean, and variance of our vertical velocity estimates for each of the selected areas from Figure 5 are shown in Table 1. The mean values are similar in magnitude for the more energetic areas (KP, PAR) on the order of 10^{-6} to 10^{-5} m s^{-1}, as well as for the more quiescent areas (IOG, POG) on the order of 10^{-7} m s^{-1}. However, due to the heavy-tailed distributions, all of the mean values depend on the particular sampling scheme selected, even for large sample sizes, so these average results must be interpreted with caution. The differences in variance are more illuminating. In the ocean gyres, the variance of our estimates are on the order of 10^{-10} [m s^{-1}]^2 while the topographic features have a variance nearer to 10^{-8} and 10^{-9} [m s^{-1}]^2 for PAR and KP, respectively. This
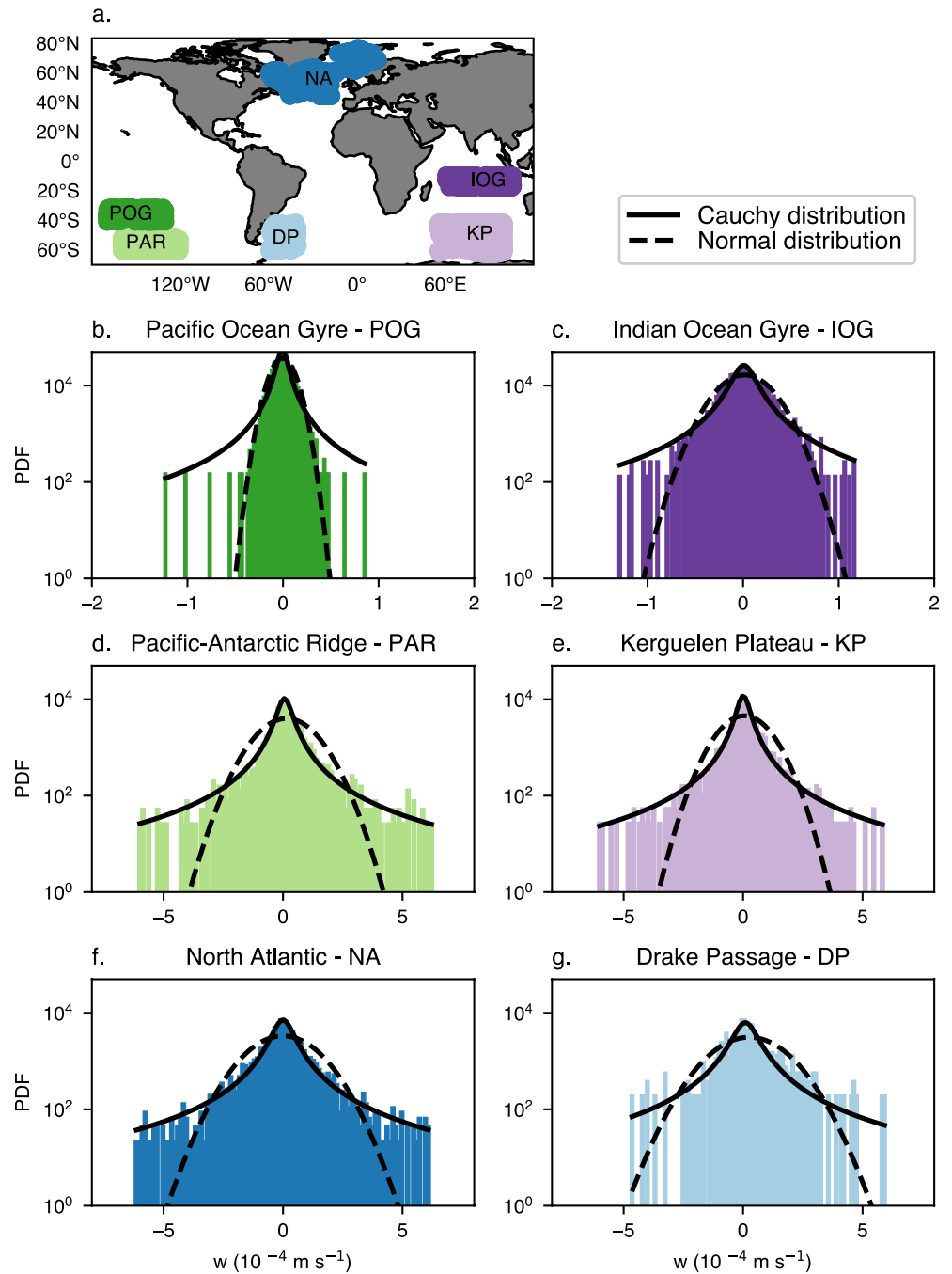
Figure 5. Probability density function distributions with Normal and Cauchy distribution functions plotted on top for select areas highlighted by corresponding color in a global map (a). (b) Pacific Ocean Gyre (POG) with 3,143 observations (dark green), (c) Indian Ocean Gyre (IOG) with 3,001 observations (dark purple), (d) Pacific-Antarctic Ridge (PAR) with 3,053 observations (light green), (e) Kerguelen Plateau (KP) with 3,057 observations (light purple), (f) North Atlantic (NA) with 3,664 observations (dark blue), (g) Drake Passage (DP) with 487 observations (light blue). Note that the *x* axis limits on panels (b) and (c) are decreased by a factor of 4 from the other PDFs.

emphasizes the impact that the high-magnitude, heavy tails have in areas with significant bathymetry. As another large topographic feature in the ACC, we expect to see a similar pattern for Drake Passage (DP) (Figure 5g). Though the estimates in this area are sparser than in the others, the variance is once again two orders of magnitude larger than those of the ocean gyres and comparable to the other active regions. The scale of the global variance is approximately 10^{-9} [m s^{-1}]^2, showing the impact of the large vertical velocities that are localized in space.

Table 1
Aggregate Statistics—Median, Mean (μ), Variance (σ²), and Ratio of Mean to Standard Deviation (μ/σ)—of Vertical Velocity Estimates Globally and for Selected Areas Shown in Figure 5

Area	Median (m s^{-1})	μ (m s^{-1})	σ^2 ([m s^{-1}]^2)	$|\mu|/\sigma$
Global	$(1.3 \pm 0.2) \times 10^{-7}$	$(1.9 \pm 0.02) \times 10^{-6}$	$(3.0 \pm 0.01) \times 10^{-9}$	0.03
KP	$(1.2 \pm 0.2) \times 10^{-6}$	$(5.4 \pm 0.2) \times 10^{-6}$	$(7.8 \pm 0.09) \times 10^{-9}$	0.06
IOG	$(7.3 \pm 1.4) \times 10^{-7}$	$(8.5 \pm 0.7) \times 10^{-7}$	$(4.5 \pm 0.05) \times 10^{-10}$	0.04
PAR	$(7.4 \pm 0.2) \times 10^{-6}$	$(1.4 \pm 0.02) \times 10^{-5}$	$(1.0 \pm 0.01) \times 10^{-8}$	0.14
POG	$(-6.2 \pm 0.9) \times 10^{-7}$	$(-4.7 \pm 0.4) \times 10^{-7}$	$(1.2 \pm 0.01) \times 10^{-10}$	0.04
DP	$(1.1 \pm 0.1) \times 10^{-5}$	$(2.5 \pm 0.07) \times 10^{-5}$	$(1.7 \pm 0.03) \times 10^{-8}$	0.19
NA	$(-1.2 \pm 0.3) \times 10^{-6}$	$(-6.1 \pm 2.3) \times 10^{-7}$	$(1.5 \pm 0.01) \times 10^{-8}$	0.005

Another area of interest is the North Atlantic (NA, Figure 5f), where the vertical velocity distribution is similar to the high energy areas of the Southern Ocean. As a region with mixed layers exceeding 1,000 m, deep water formation, and significant eddy activity (Ferrari & Wunsch, 2009; Stommel & Arons, 1959), it is expected that the NA mimics the other active regions. Indeed, the variance is once again two orders of magnitude larger than that of the quiescent areas.

The median values of our vertical velocity estimates range from 10^{-7} to 10^{-5} m s^{-1} (Table 1). The larger values occur in high energy areas while the smaller values occur in the gyres. The global median is on the same order of magnitude as the gyre median values. This shows that, though the effects of large-magnitude events can be seen in the global variance, the small-magnitude phenomena that form the high peak in the distribution dominate the median (and mean).

The substantial impact of variability in mesoscale vertical velocities is further emphasized by the ratio of the absolute value of the mean and the standard deviation ($|\mu|/\sigma$, Table 1, Column 5), which varies between 0.005 and 0.19. In the gyre regions, this ratio is close to the global average value of 0.03, while the largest values are found in the energetic Southern Ocean areas.

Interestingly, the NA and POG both have a negative average vertical velocity, suggesting mean downwelling across 1,000 m in these regions. Although the mean velocities are quite comparable, the observed variance is two orders of magnitude larger in the NA than in the POG. Given the resulting small ratio between the absolute value of the mean and the standard deviation (0.005 in the NA compared to 0.04 in the POG), we abstain from a physical interpretation of the negative mean vertical velocity in the NA. However, the larger ratio in the POG and the fact that the velocities there are more normally distributed (see discussion in Section 4.3) imply that the estimate of the mean in that region is more robust.

Considering a steady-state, one-dimensional balance between advection and diffusion in the temperature equation (Tsujino et al., 2000),

$$w\frac{\partial T}{\partial z} = \frac{\partial}{\partial z}\left(K_v \frac{\partial T}{\partial z}\right), \tag{6}$$

we can examine the implications of an average downward vertical velocity, which is contrary to the canonical model put forth by Munk (1966). Near 1,000 m, the first- and second-order vertical derivatives of temperature are positive (generally and in the POG specifically), and assuming down-gradient diffusion of heat gives a strictly positive value for vertical diffusivity (K_v). Therefore, in this one-dimensional model, a mean downward vertical velocity could only arise due to a negative gradient in diffusivity, implying an increase in mixing in the deeper waters relative to shallower depths. Such a vertical gradient in diffusivity at 1,000 m has been shown to be necessary for models to more accurately replicate deep Pacific circulation (Tsujino et al., 2000).

The SLA associated with our select areas also highlight the variability between different locations. The SLA in the IOG and POG (Figures 6a and 6b) are similar in range going from −0.33 to 0.35 m with small vertical velocities. However, the SLA in the PAR (Figure 6c) is more limited ranging only between −0.11 and 0.15 m with larger vertical velocities. The SLAs near the KP (Figure 6d) are again different to those at IOG/POG and PAR, showing a wide range for both SLA (−0.49 to 0.41 m) and vertical velocity. This reinforces that there is
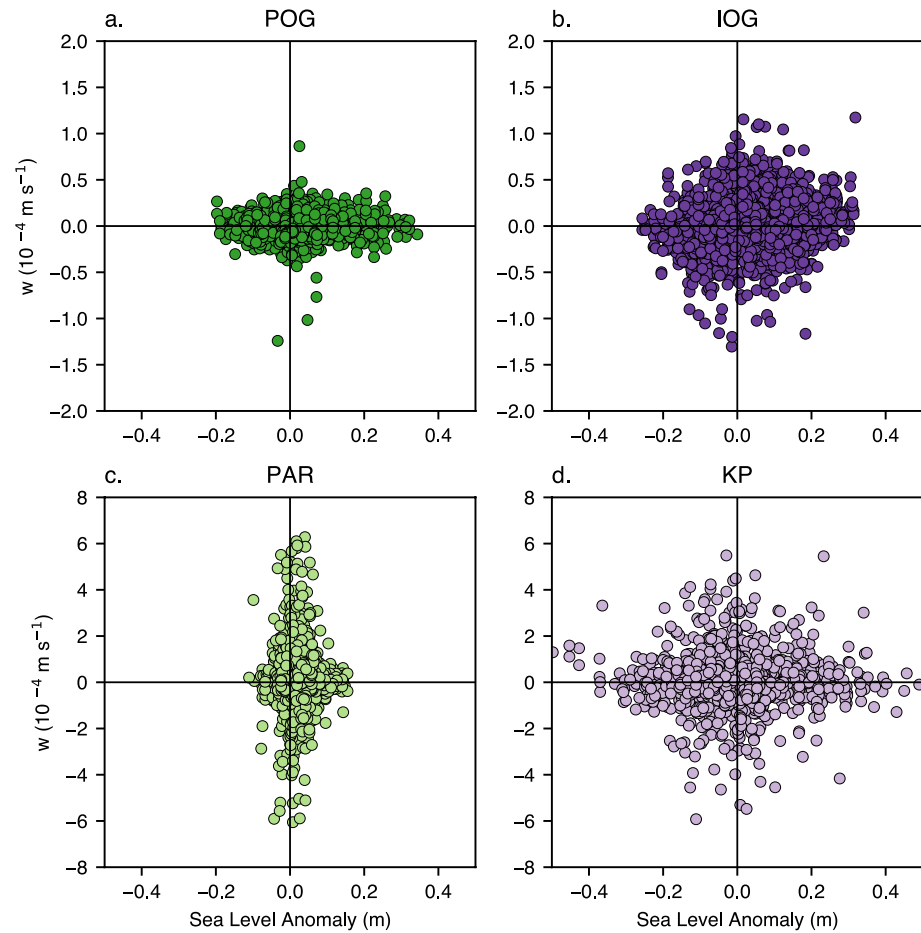
Figure 6. Data Unification and Altimeter Combination System Sea Level Anomaly at the nearest grid point averaged over time of corresponding half cycles (as described in Section 4.2) versus vertical velocity estimates for select areas highlighted by corresponding color in a global map in Figure 5a. (a) Pacific Ocean Gyre (POG) (dark green), (b) Indian Ocean Gyre (IOG) (dark purple), (c) Pacific-Antarctic Ridge (PAR) (light green), (d) Kerguelen Plateau (KP) (light purple). Note that the *y* axis limits on panels (a) and (b) are decreased by a factor of 4 from panels (c) and (d).

high variability in the spatial distribution of vertical velocities that are interacting with a variety of mechanisms, even in similarly energetic regimes.

4.4. Effects of Bathymetry and Horizontal Flow

To examine other factors that may impact the observed vertical velocity variability, we utilize the satellite derived horizontal velocities (as described in Section 4.2) and the ETOPO1 1 Arc Minute Global Relief Model (Amante & Eakins, 2009; NGDC, 2009). We use the version of bathymetry that includes the bases of the Antarctic and Greenland ice sheets. To better compare between the gridded relief model and the Argo array, we located the nearest grid cell to each float cycle location that contains an ocean depth. Because bathymetry changes on time scales much longer than the mesoscale phenomena we are focused on, we assume that the bathymetry remains constant.

Examining both the global surface velocities and the ocean bathymetry with their corresponding float *w* estimates, we see that deep areas with small horizontal surface velocities tend to have smaller values of *w*. However, areas with larger average horizontal surface flow (>0.08 m s^{-1}) have more high magnitude vertical velocities, even where the ocean is deep (between 4,000 and 5,000 m) (Figure 7). Prior research has shown elevated mesoscale eddy activity frequently occurs downstream of strong horizontal flows crossing over topographic features (Cusack et al., 2017; Liang et al., 2017; Rosso et al., 2014). This lag between the peak in bathymetry and the peak in vertical velocity may also contribute to high magnitude vertical velocities occurring where the ocean is deeper.
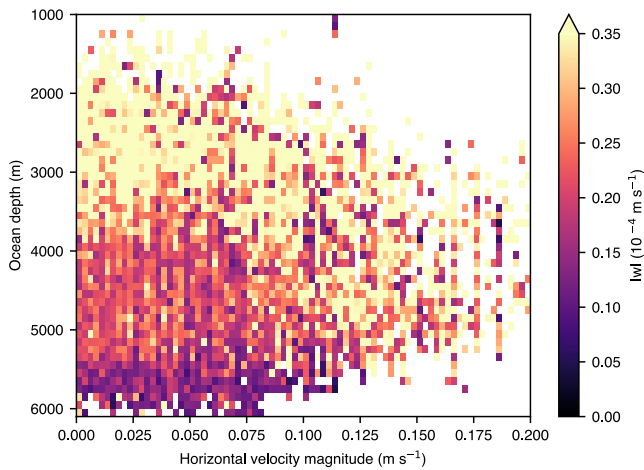
Figure 7. Average absolute value vertical velocity within grid cells of horizontal surface velocity averaged over 1993–2020 (bin size of 0.0025 m s^{-1}) and ocean depth (bin size of 75 m). Only grid cells with at least five estimates of vertical velocity are shown here. Note that floats are typically not deployed in waters shallower than 2,000 m (due to a desire to prevent float grounding) so sparseness in samples above this depth is expected.

To analyze how the vertical velocity signal relates to bathymetry as the ocean flows across topographic features, we will highlight the ACC as a case study. This area is characterized by a strong zonal flow across several notable topographic features (Tamsitt et al., 2017; Yung et al., 2022) (Figure 8b) and it includes adequate float coverage across most longitudes except in the Atlantic Ocean. Consistent with the results discussed in Section 4.3, hot spots of vertical velocity magnitude correspond roughly to known bathymetric features in the path of the ACC, including KP, PAR, and DP as well as Macquarie Ridge and the Southwest Indian Ridge (Tamsitt et al., 2017; Yung et al., 2022).

Here we define the ACC area as the polygon bounded by the zonally continuous streamfunction contours −0.7 to 3.4 dynamic m, as computed from Argo floats by Zilberman et al. (2023) (Figure 8a). We have taken all of the vertical velocity data within the ACC, and computed a running average with 4° longitude boxes at a 2° longitude spacing. We then did the same for all of the bathymetry data included in the ACC polygon. Finally, we compute a normalized lagged correlation between average ocean bottom depth and average absolute vertical velocity for areas with greater than 15 samples and get that they are somewhat correlated ($r = 0.55$) (Figure 8b). The vertical velocity peaks lag the bathymetry peaks by approximately 9° longitude, meaning that higher magnitude values occur downstream in the ACC, as expected. However, this correlation certainly does not explain all of the variability in vertical velocity. Other factors are at play, including variable horizontal flow and multiple bathymetric features interacting with the current, particularly if features are near to one another or cover large areas.

Taken altogether, these results from the ACC indicate that at mid-depths, higher vertical velocities occur downstream of shallow bathymetry (Figure 8), which is supported by our findings of a relationship between bathymetry, horizontal flow, and vertical velocity magnitude in the global estimates (Figure 7). This provides evidence that the 5-day average vertical velocities determined from Argo observations primarily reflect mesoscale phenomena.
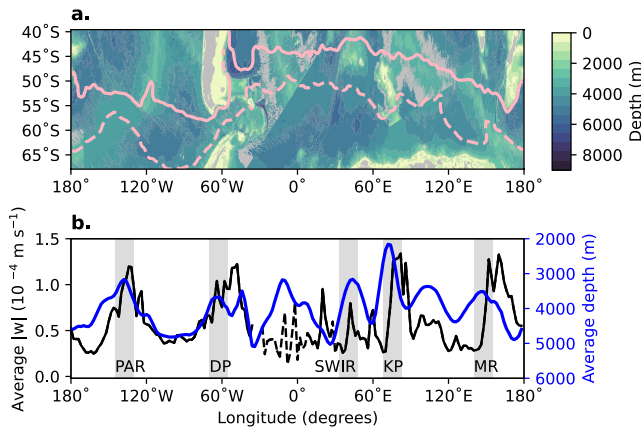
5. Discussion and Conclusions

The results presented here are the first estimates of subsurface vertical velocity determined directly from observations, across wide swaths of the global ocean. Our approach of using measurements from floats in the globally distributed Argo array provides insight into three-dimensional flows occurring near 1,000 m. The sampling distribution is uneven, with some regions well covered and others lacking data entirely, due to differences in how floats report data from the drift phase at the parking depth. As the global Argo array continues to evolve, drift data suited for this method will continue to be collected from many floats, thereby increasing the coverage of these vertical velocity estimates (Argo User's Manual, 2022; Riser et al., 2016; Roemmich et al., 2019; Wong et al., 2020). Furthermore, we encourage all float manufacturers and users to measure and report hourly temperature and pressure data during the drift phase when possible, to expand the spatial coverage of these vertical velocity estimates.

In areas with adequate sampling, our results highlight distinctive spatial variability in vertical velocities at 1,000 m. In particular, there is clear evidence of a relationship between vertical motion and topographic features, with further influence in areas with strong horizontal flows. This topographic dominance is consistent with prior global estimates of mid-depth vertical velocity using model fields (Liang et al., 2017). To better assess our estimates in relation to velocity output from a widely-used ocean state estimate, we retrieved data
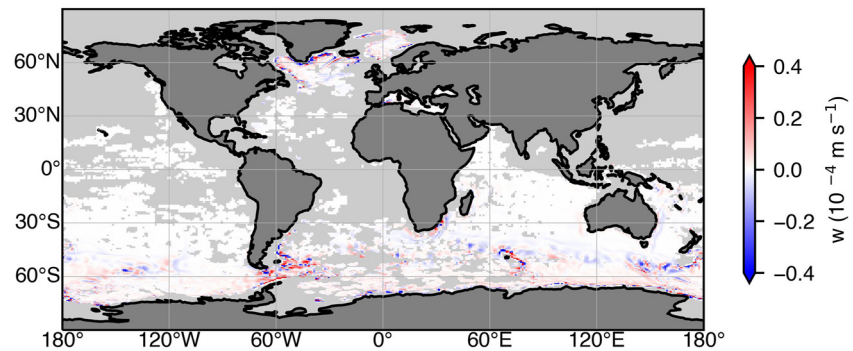

Figure 8. (a) ETOPO1 bathymetry of the Antarctic Circumpolar Current (ACC) and surrounding area. The pink lines show the streamfunction contours (−0.7 to 3.4 dynamic m, as computed by Zilberman et al. (2023)) that define the edges of the ACC. (b) (Black—left axis) Running average of absolute value vertical velocities within the ACC using 4° longitude boxes spaced every 2°, constrained in latitude by the streamfunction contours in panel (a). Note that the dashed line here refers to areas where there were fewer than 15 samples included in the average. (Blue—right axis) Running average of ETOPO1 depth within the ACC using 4° longitude boxes spaced every 2°, constrained in latitude by the streamfunction contours in panel (a). Significant topographic features highlighted with gray boxes (Pacific-Antarctic Ridge [PAR], Drake Passage [DP], Kerguelen Plateau, Southwest Indian Ridge [SWIR], and Macquarie Ridge [MR]).

Figure 9. Global map of the vertical velocity field from the ECCOv4.4 model in grid cells that contain observational estimates from floats.

from the latest Estimating the Circulation and Climate of the Ocean (ECCO) project (version 4, release 4) (Forget et al., 2015). We used the monthly-averaged vertical component of velocity from 2004 to 2017, which best over-laps with the time period available for the float estimates. We took the 1/2° resolution LLC90 grid, chose the depth level closest to 1,000 dbar, and then selected only locations that have at least one float estimate of vertical velocity within 50 km of center of the model grid-cell. Subsampling the model output in this way eliminates data from the coastal areas and shallow areas where floats do not sample.

Averaging the resulting model vertical velocity fields over the full 13-year period reveals spatial variability that matches the spatial pattern in the Argo-based estimates remarkably well. This similarity again emphasizes the topographic influence on vertical motions near 1,000 m (Figures 2 and 9). The ECCO vertical velocities in Figure 9 are an order of magnitude smaller than the float-based velocities in Figure 2, reflecting the difference in the temporal scales of the two estimates and highlighting the influence from the spatial resolution of the model.

Examining instead the monthly-averaged velocities from ECCOv4.4, again restricted to only the locations of the float estimates, the normalized distribution of vertical velocity exhibits a high peak and heavy tails that is best fit by the Cauchy distribution, like the float-based estimates (Figure 10).

Although the 5-day averaged float estimates and the monthly model w fields still have different temporal scales, the similarity in the shape of the distributions provides support for the efficacy of the vertical velocity estimation method described here. Interestingly, the distribution of the observational w estimates is more symmetric than the distribution of the model vertical velocities, which is skewed toward negative values. Possible reasons for this include the uneven temporal spacing in the float estimates when compared to the model field or inadequate representation of mesoscale motions in the model. In addition, the tails of the float-based distribution decrease
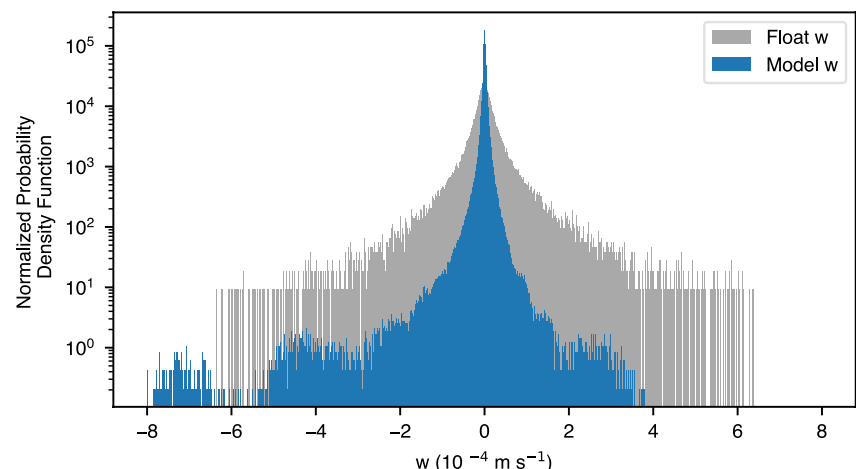

Figure 10. Distributions of model vertical velocity (blue) and observational estimates (gray), with each bin showing the count in the bin divided by the total number of observations and by the bin size (1×10^{-6} m s^{-1}).

monotonically, while the model-based distribution exhibits multiple local maxima in both tails, likely due to limitations of the model's vertical resolution (Forget et al., 2015; Liang et al., 2017; Wong et al., 2020).

Advecting a synthetic float using model velocity fields and then recreating our vertical velocity estimation procedure might appear to be an ideal way to validate this technique. Unfortunately, the spatial and temporal scales required to accurately represent all the relevant dynamics, from the float interactions with the surrounding waters to oceanic mesoscale features, are immensely challenging to achieve (Liang et al., 2017; Swift & Riser, 1994; Wang et al., 2020). Thus a direct model-based validation of the method developed here remains outside the scope of this work.

The direct estimates of 1,000-m vertical velocity given here would not be possible without high-frequency data from the parking phase of Argo profiling floats. Though measuring vertical velocities was not an original intention of the Argo program (Riser et al., 2016; Roemmich et al., 2019), being able to adapt this globally-distributed in situ observational data set for novel methods such as the one presented here has immensely increased its scientific value. Continued improvements in float technology will allow for refinement and expansion of this method, as well as the development of others. These capabilities are made possible by the dedicated efforts of the international Argo program to ensure that all float data (i.e., trajectory, technical, metadata, and profile data) are provided in a consistent, quality-controlled format.

The estimates of w computed here directly from Argo float drift observations fit well within the range of values given by prior studies (Cusack et al., 2017; Freeland, 2013; Liang et al., 2017; Martin & Richards, 2001; Pilo et al., 2018; Stommel & Arons, 1959). The distribution of these velocities, characterized by a narrow peak and heavy tails, emphasizes the distinctly non-Gaussian nature of vertical flows in the interior ocean. The variability in 5-day average w near 1,000 m revealed here provides widespread direct observation-based evidence of the importance of topographic interactions in generating strong vertical motions at the oceanic mesoscale. This novel application of the Argo data set greatly expands our knowledge of the subsurface circulation of the global ocean and provides a unique observational constraint for model validation.

Data Availability Statement

Float data were collected and made freely available (https://www.seanoe.org/data/00311/42182/) by the International Argo Program and the national programs that contribute to it (https://argo.ucsd.edu, https://www.ocean-ops.org) (Argo, 2000). The Argo Program is part of the Global Ocean Observing System.

Bathymetry data from the ETOPO1 1 Arc Minute Global Relief Model are openly available via https://doi.org/10.25921/fd45-gt74 (NGDC, 2009). Sea level anomaly and surface horizontal velocities were obtained from the DUACS L4 gridded altimeter product and are available via https://doi.org/10.48670/moi-00148 (CMEMS, 2021). Model data from the ECCO project (v4r4) are available from the ECCO data server via https://ecco.jpl.nasa.gov/drive/files/Version4/Release4/ (Fukumori et al., 2019).

The Jupyter Notebook to execute the analysis and create figures in the paper can be found at https://github.com/katychris/Christensen2023_w_estimates/tree/v1.0.1, is hosted at GitHub, and is preserved at DOI: 10.5281/zenodo.10358307 under a standard MIT license (Christensen, 2023).

References

Amante, C., & Eakins, B. W. (2009). Etopo1 arc-minute global relief model: Procedures, data sources and analysis. NOAA Technical Memorandum NESDIS NGDC-24.

Argo. (2000). Argo float data and metadata from Global Data Assembly Centre (Argo GDAC) [Dataset]. SEANOE. https://doi.org/10.17882/42182

Argo User's Manual. (2022). Report (Normative document). https://doi.org/10.13155/29825

Assassi, C., Morel, Y., Vandermeirsch, F., Chaigneau, A., Pegliasco, C., Morrow, R., et al. (2016). An index to distinguish surface- and subsurface-intensified vortices from surface observations. *Journal of Physical Oceanography*, *46*(8), 2529–2552. https://doi.org/10.1175/JPO-D-15-0122.1

Christensen, K. M. (2023). Christensen 2023 w estimates (version 1.0.1) [Software]. Zenodo. https://doi.org/10.5281/zenodo.10358307

CMEMS. (2021). Global ocean gridded L4 sea surface heights and derived variables reprocessed (1993-ongoing) [Dataset]. https://doi.org/10.48670/moi-00148

Cusack, J. M., Naveira Garabato, A. C., Smeed, D. A., & Girton, J. B. (2017). Observation of a large Lee wave in the Drake Passage. *Journal of Physical Oceanography*, *47*(4), 793–810. https://doi.org/10.1175/JPO-D-16-0153.1

Ferrari, R., & Wunsch, C. (2009). Ocean circulation kinetic energy: Reservoirs, sources, and sinks. *Annual Review of Fluid Mechanics*, *41*(1), 253–282. https://doi.org/10.1146/annurev.fluid.40.111406.102139

Forbes, C., Evans, M., Hastings, N., & Peacock, B. (2010). Cauchy distribution. In *Statistical distributions* (pp. 66–68). John Wiley & Sons, Ltd. https://doi.org/10.1002/9780470627242.ch10

Forget, G., Ferreira, D., & Liang, X. (2015). On the observability of turbulent transport rates by Argo: Supporting evidence from an inversion experiment. *Ocean Science*, *11*(5), 839–853. https://doi.org/10.5194/os-11-839-2015

Frajka-Williams, E., Eriksen, C. C., Rhines, P. B., & Harcourt, R. R. (2011). Determining vertical water velocities from Seaglider. *Journal of Atmospheric and Oceanic Technology*, *28*(12), 1641–1656. https://doi.org/10.1175/2011JTECHO830.1

Freeland, H. J. (2013). Vertical velocity estimates in the North Pacific using Argo floats. *Deep-Sea Research Part II: Topical Studies in Oceanography*, *85*, 75–80. https://doi.org/10.1016/j.dsr2.2012.07.019

Fritsch, F. N., & Carlson, R. E. (1980). Monotone piecewise cubic interpolation. *SIAM Journal on Numerical Analysis*, *17*(2), 238–246. https://doi.org/10.1137/0717021

Fukumori, I., Wang, O., Fenty, I., Forget, G., Heimbach, P., & Ponte, R. M. (2019). ECCO version 4 release 4 [Dataset]. Retrieved from https://ecco.jpl.nasa.gov/drive/files/Version4/Release4/doc/v4r4_synopsis.pdf

Hennon, T. D., Riser, S. C., & Alford, M. H. (2014). Observations of internal gravity waves by Argo floats. *Journal of Physical Oceanography*, *44*(9), 2370–2386. https://doi.org/10.1175/jpo-d-13-0222.1

Liang, X., Spall, M., & Wunsch, C. (2017). Global ocean vertical velocity from a dynamically consistent ocean state estimate. *Journal of Geophysical Research: Oceans*, *122*(10), 8208–8224. https://doi.org/10.1002/2017JC012985

Martin, A. P., & Richards, K. J. (2001). Mechanisms for vertical nutrient transport within a North Atlantic mesoscale eddy. *Deep-Sea Research Part II: Topical Studies in Oceanography*, *48*(4–5), 757–773. https://doi.org/10.1016/S0967-0645(00)00096-5

McDougall, T., & Barker, P. (2011). *Getting started with TEOS-10 and the Gibbs Seawater (GSW) Oceanographic Toolbox* (p. 28). SCOR/IAPSO WG127.

Merckelbach, L., Smeed, D., & Griffiths, G. (2010). Vertical water velocities from underwater gliders. *Journal of Atmospheric and Oceanic Technology*, *27*(3), 547–563. https://doi.org/10.1175/2009JTECHO710.1

Munk, W. H. (1966). Abyssal recipes. *Deep-Sea Research and Oceanographic Abstracts*, *13*(4), 707–730. https://doi.org/10.1016/0011-7471(66)90602-4

NGDC. (2009). ETOPO1 1 arc-minute global relief model [Dataset]. NOAA National Centers for Environmental Information. https://doi.org/10.25921/fd45-gt74

Pilo, G. S., Oke, P. R., Coleman, R., Rykova, T., & Ridgway, K. (2018). Patterns of vertical velocity induced by eddy distortion in an ocean model. *Journal of Geophysical Research: Oceans*, *123*(3), 2274–2292. https://doi.org/10.1002/2017JC013298

Pujol, M.-I., Faugère, Y., Taburet, G., Dupuy, S., Pelloquin, C., Ablain, M., & Picot, N. (2016). DUACS DT2014: The new multi-mission altimeter data set reprocessed over 20 years. *Ocean Science*, *12*(5), 1067–1090. https://doi.org/10.5194/os-12-1067-2016

Riser, S. C., Freeland, H. J., Roemmich, D., Wijffels, S., Troisi, A., Belbéoch, M., et al. (2016). Fifteen years of ocean observations with the global Argo array. *Nature Climate Change*, *6*(2), 145–153. https://doi.org/10.1038/nclimate2872

Roemmich, D., Alford, M. H., Claustre, H., Johnson, K. S., King, B., Moum, J., et al. (2019). On the future of Argo: A global, full-depth, multi-disciplinary array. *Frontiers in Marine Science*, *6*(JUL), 1–28. https://doi.org/10.3389/fmars.2019.00439

Rosso, I., Hogg, A. M., Strutton, P. G., Kiss, A. E., Matear, R., Klocker, A., & van Sebille, E. (2014). Vertical transport in the ocean due to sub-mesoscale structures: Impacts in the Kerguelen region. *Ocean Modelling*, *80*, 10–23. https://doi.org/10.1016/j.ocemod.2014.05.001

Sévellec, F., Naveira Garabato, A. C., Brearley, J. A., & Sheen, K. L. (2015). Vertical flow in the Southern Ocean estimated from individual moorings. *Journal of Physical Oceanography*, *45*(9), 2209–2220. https://doi.org/10.1175/JPO-D-14-0065.1

Stommel, H., & Arons, A. B. (1959). On the abyssal circulation of the world ocean - II. An idealized model of the circulation pattern and amplitude in oceanic basins. *Deep Sea Research (1953)*, *6*(C), 217–233. https://doi.org/10.1016/0146-6313(59)90075-9

Sugiyama, M. (2016). Chapter 4 - Examples of continuous probability distributions. In M. Sugiyama (Ed.), *Introduction to statistical machine learning* (pp. 37–50). Morgan Kaufmann. https://doi.org/10.1016/B978-0-12-802121-7.00015-7

Sverdrup, H. U. (1947). Wind-driven currents in a baroclinic ocean; with application to the equatorial currents of the eastern pacific. *Proceedings of the National Academy of Sciences*, *33*(11), 318–326. https://doi.org/10.1073/pnas.33.11.318

Swift, D., & Riser, S. (1994). Rafos floats: Defining and targeting surfaces of neutral buoyancy. *Journal of Atmospheric and Oceanic Technology*, *11*(4), 1079–1092. https://doi.org/10.1175/1520-0426(1994)011<1079:RFDATS>2.0.CO;2

Tamsitt, V., Drake, H. F., Morrison, A. K., Talley, L. D., Dufour, C. O., Gray, A. R., et al. (2017). Spiraling pathways of global deep waters to the surface of the Southern Ocean. *Nature Communications*, *8*(1), 1–10. https://doi.org/10.1038/s41467-017-00197-0

Tsujino, H., Hasumi, H., & Suginohara, N. (2000). Deep pacific circulation controlled by vertical diffusivity at the lower thermocline depths. *Journal of Physical Oceanography*, *30*(11), 2853–2865. https://doi.org/10.1175/1520-0485(2001)031<2853:dpccbv>2.0.co;2

Wang, T., Gille, S. T., Mazloff, M. R., Zilberman, N. V., & Du, Y. (2020). Eddy-induced acceleration of Argo floats. *Journal of Geophysical Research: Oceans*, *125*(10), e2019JC016042. https://doi.org/10.1029/2019jc016042

Wong, A. P., Wijffels, S. E., Riser, S. C., Pouliquen, S., Hosoda, S., Roemmich, D., et al. (2020). Argo data 1999–2019: Two million temperature-salinity profiles and subsurface velocity observations from a global array of profiling floats. *Frontiers in Marine Science*, *7*(September), 1–23. https://doi.org/10.3389/fmars.2020.00700

Yung, C. K., Morrison, A. K., & Hogg, A. M. (2022). Topographic hotspots of Southern Ocean eddy upwelling. *Frontiers in Marine Science*, *9*, 855785. https://doi.org/10.3389/fmars.2022.855785

Zilberman, N., Scanderbeg, M., Gray, A., & Oke, P. (2023). Scripps Argo trajectory-based velocity product: Global estimates of absolute velocity derived from core, biogeochemical, and deep Argo float trajectories at parking depth. *Journal of Atmospheric and Oceanic Technology*, *40*(3), 361–374. https://doi.org/10.1175/jtech-d-22-0065.1